Solution Synthesized Extended Graphene Nanoribbons Deposited by High-vacuum Electrospray Deposition

Sebastian Scherb,[*,†] Antoine Hinaut,[†] Xuelin Yao,[‡] Alicia Götz,[‡,¶] Samir H. Al-Hilfi,[‡] Xiao-Ye Wang,[‡] Yunbin Hu,[‡] Zijie Qiu,[‡] Yiming Song,[†] Klaus Müllen,[‡,¶] Thilo Glatzel,[†] Akimitsu Narita,[‡] and Ernst Meyer[*,†]

†*Department of Physics, University of Basel, Klingelbergstrasse 82, 4056, Basel, Switzerland*

‡*Max Plank Institute for Polymer Research, Ackermannweg 10, 55128, Mainz, Germany*

¶*Department of Chemistry, Johannes Gutenberg University Mainz, Duesbergweg 10-14, 55128 Mainz, Germany*

* E-mail: sebastian.scherb@unibas.ch; ernst.meyer@unibas.ch

Abstract

Solution synthesized graphene nanoribbons (GNRs) facilitate various interesting structures and functionalities, like non-planarity and thermolabile functional groups, that are not or not easily accessible by on-surface synthesis. Here, we show the successful high-vacuum electrospray deposition (HVESD) of well-elongated solution synthesized GNRs on surfaces maintained in ultra-high vacuum. We compare three distinct GNRs, a twisted non-planar fjord-edged GNR, a methoxy-functionalized "cove"-type (or also called gulf) GNR and a longer "cove"-type GNR both equipped with alkyl chains on Au(111). Nc-AFM measurements at room temperature with submolecular imaging combined with Raman spectroscopy allow us to characterize individual GNR and confirm their chemical integrity. The fjord-GNR and methoxy-GNR are additionally deposited on non-metallic HOPG, SiO_2 and fjord-GNR on KBr(001) surface, facilitating the study of GNRs on substrates, as of now not accessible by on-surface synthesis.

Keywords

Graphene nanoribbons, Electrospray deposition, nc-AFM, non-planarity, solution synthesis

Graphene nanoribbons (GNRs), thin quasi-one-dimensional strips of graphene, have attracted immense interest due to their intriguing electronic properties.[1–4] Size confinement along one direction, the possibility to incorporate heteroatoms or the fine control of their edges allow tuning their electronic properties.[5–8] So far, on-surface synthesis is the most advanced method to obtain well-defined and atomically precise GNR on surfaces.[8,9] In general, precursor molecules bearing bromo or iodo groups are deposited on a metal surface followed by heat treatment. After the cleavage of the carbon-halogen bond, the resulting diradical intermediates undergo polymerization and cyclodehydrogenation reactions leading

to well-defined GNRs. Modulation of the edge structure and the inclusion of heteroatoms are achieved by careful design of the precursor molecules allowing GNRs to present tunable properties.[2,5,8,10–14] The well-defined structures of obtained GNRs and the cleanliness of the surface make this fabrication of GNR suitable for high-resolution scanning probe investigations permitting characterization at local scale for fundamental studies. However, on-surface synthesis is usually limited by the need for a metal surface,[15–17] thus restricting studies of the electronic properties due to coupling to the conducting surface. The deposition of thin layers of insulating materials and subsequent transfer of GNRs from the metallic substrate by tip induced manipulation or the admixture of insulating material to the top layers of the substrate can be employed to mitigate this limitation.[13,18–20] Additionally, some approaches have been achieved which expand the on-surface synthesis to further surfaces.[17]

Compared to the on-surface method, solution synthesis offers interesting advantages.[21–24] First, the scalability of the method allows larger quantities to be produced. Moreover, solution synthesis can lead to the formation of very long GNRs and allow for the controlled incorporation of functional groups on the edges. Another advantage is the possibility to avoid metal surfaces. Interestingly, 3D-shaped GNRs can be prepared,[6,25–29] which are not readily accessible through on-surface synthesis.[30] Avoiding annealing steps also allows the implementation of additional heteroatoms, anchoring or functional groups that are not stable at high temperatures. However, the elucidation of the precise chemical structures of such GNRs has remained challenging in many cases. Until now, the major limitation of high-resolution studies of solution synthesized GNR has been the safe and clean transfer to surfaces. Depositions have successfully been performed by droplet casting[31] and more recently by direct transfer.[32] With the application of Matrix-Assisted Direct (MAD) transfer a hybrid approach has allowed the implementation of on-surface synthesis for well elongated polymer precursors to form GNR on surface.[33]

High vacuum electrospray deposition (HVESD) allows transferring molecular species from solution to surfaces maintained in ultra-high vacuum (UHV) conditions with cleanliness

allowing high-resolution scanning probe studies.[34–37] HVESD is an in line setup based on electrospray deposition,[38–46] where no selection of the introduced species is necessarily performed. An advantage is the option to introduce species with broad mass distribution from a single solution. The possibility to work with non-conducting substrates is also important to study the properties of adsorbates decoupled from metals.[34,47]

Here, we show the successful HVESD of well-elongated GNRs on different surfaces maintained in UHV conditions. We provide comparison of three solution synthesized GNRs exhibiting different average lengths, functional groups and alkyl side chains. Notably, this includes non-planar fjord-edged GNR (FGNR) decorated with *tert*-butyl groups, methoxy-functionalized GNR with "cove"-type (also called gulf) edges (OMeCGNR) equipped with dodecyl alkyl chains for solubility, and longer GNR with the same structure but without the methoxy groups (CGNR) with their chemical structure visible in Figs. 1a-c, respectively. The characterization is performed by non-contact atomic force microscopy (nc-AFM) at room temperature (RT) providing large scale overviews of the GNRs and confirming the length distribution of the different nanoribbons. Nc-AFM studies reveal a more flexible and twisted structure for FGNR, providing evidence of a non-planar, twisted GNR, while a more rigid and straight planar structure is observed for the OMeCGNR and the CGNR. The chemical integrity of the observed species is verified by Raman spectroscopy[9,48–51] performed after ESD, providing proof that the GNRs successfully deposited. In addition, we achieved the deposition of FGNR and OMeCGNR on non-metallic surfaces. Raman spectra after deposition on HOPG, SiO_2 and for FGNR on bulk insulator KBr(001) confirms the deposition of GNRs on such surfaces. Nc-AFM imaging of FGNR on HOPG and KBr(001) shows formation of isolated or clustered GNR structures with some influence on surface morphology. Together with the possibility of obtaining clean surfaces without any post-deposition annealing procedure and their stabilization at room temperature, this allows using GNRs with more fragile structure, for needs where high temperature should be avoided on materials where their intrinsic properties can be studied.

Results

Comparison of three types of GNR on Au(111).

HVESD results in a homogeneous dispersed distribution of GNR on the Au(111) surfaces, as observed for FGNR, OMeCGNR and CGNR in large topography images shown in Figs. 1d-f, respectively. There, large scale terraces of Au(111) with bright, elongated structures, corresponding to the GNRs are observed. The FGNRs and OMeCGNRs are isolated from each other and present a similar length as seen in Figs. 1d and e. The much longer CGNRs are sometimes overlapping and as expected are up to one order of magnitude more extended, as seen in Fig. 1f.[52] Distribution measurement show an average length value of 21 ± 11 nm for FGNR, as shown in the histogram of Fig. 1g, in good agreement with expected length estimated from molecular weight based on size-exclusion chromatography analysis of the corresponding polyphenylene precursor.[29] Length distribution of 20 ± 7 nm for OMeCGNR and 80 ± 34 nm for CGNR are obtained and displayed in the histograms of Figs. 1h-i. The latter also being in good agreement with previous length measurements.[52] Since synthesizing GNR with exact length is difficult, our observations of such distributions show the power of the HVESD device to allow studying such broad mass molecular species.

Noticeable adsorption differences are observed between FGNR and OMeCGNR. FGNRs are more isolated and some wiggling in their elongated orientation is already visible at the large scale – Fig. 1d. OMeCGNRs are fully straight and can form structures where few GNRs align parallel to each others. Still, the separation distance between OMeCGNRs in such structures remains visible indicating the absence of alkyl chain intercalation.[36,53] Solvent is also observed for the FGNRs, as periodically aligned protrusions visible in Fig. 1d. Their position correlates with the elbows of the herringbone reconstruction (HB), marked by the dashed lines, acting as a preferential adsorption site to trap the solvent molecules.[47] Most of the FGNRs are also aligned along those elbows, indicating that they are oriented across the HB reconstruction. This is confirmed in the contrast modified topography image in Figure S1

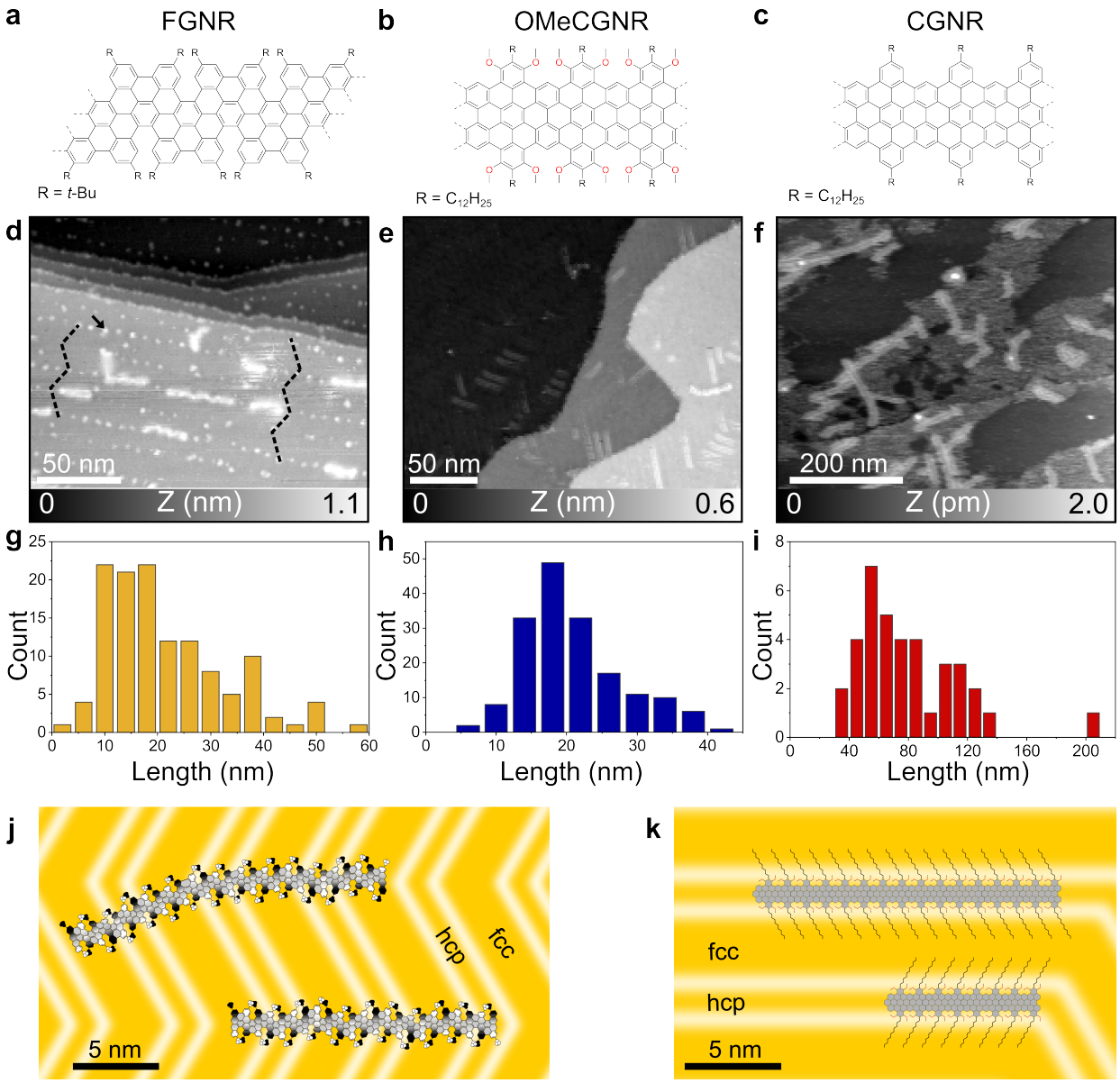

Figure 1: **GNRs on Au(111). a,** Chemical structures of FGNR, **b,** of OMeCGNR and **c,** of CGNR. **d,** Large scale nc–AFM topography of FGNRs on Au(111). ($f_1 = 174.59$ kHz, $A_1 = 3$ nm, $\Delta f_1 = -20$ Hz). **e,** Large scale nc–AFM topography of OMeCGNRs on Au(111). ($f_2 = 1.037$ MHz, $A_2 = 1.2$ nm, $\Delta f_2 = -15$ Hz). **f,** nc-AFM topography image of CGNRs. ($f_1 = 160.01$ kHz, $A_1 = 5$ nm, $\Delta f_1 = -7$ Hz). **g,** Length distribution of FGNRs, **h,** OMeCGNRs, and **i,** CGNRs. **j,** Model of the adsorption across the herringbone reconstruction based on FGNRs in Figs. 1d and 2a. The coloring corresponds to the relative height in respect to the surface. **k,** Model of the adsorption of OMeCGNR along the HCP domain of the herringbone reconstruction.

of the Supporting Information (SI), where the HB can be distinguished and the position of FGNR and pollutants observed. An illustration of the ribbon position is presented in Fig. 1j.

OMeCGNRs, on the other hand, are aligned with the HB and follow the hcp/fcc structures, as visible in the topography image in Fig. 1e. SI Fig. S2 shows that the GNR core is aligned along the hexagonal close-packed (hcp) domain of the HB, as illustrated in the model in Fig. 1k.

The CGNRs present a significantly different adsorption compared to FGNRs and OMeCGNRs. The large scale topography in Fig. 1f shows the well elongated structures of the CGNR with length up to 200 nm. The GNRs show no specific alignment to the herringbone and show mostly relatively straight structures with only slight turns visible. Interestingly, they intersect close to each other at certain points on the surface, either due to interactions or more likely due to clustering and the limited space during the deposition. Also visible on, below or around the GNRs, mobile and unstable areas, can be attributed to solvent, whereas, the more flat and stable region correspond to the uncovered surface. The solvent coverage is increased for the CGNR likely due to a higher solvent flux during deposition necessitated by low solubility observed for the CGNRs. More clear identification of the different surface areas is possible with help of the excitation image presented in the SI Fig. S3.

To more closely study the differences of the GNRs due to their various edge functionalizations, close-up images along with submolecular resolution studies were performed on single nanoribbons. An isolated FGNR is shown on the Au(111) surface in the nc-AFM topography image of Fig. 2a. Prominently visible is the highly wiggly structure of FGNR observed by the turns and kinks in the molecule. This indicates an important intramolecular flexibility due to its fjord-edge structure and also points towards the predicted bending of the nanoribbon leading to a non-planar structure.[29] In plane bending of GNRs has previously been reported due to tip induced manipulation and at the air-liquid interface,[22,54] the twists in FGNR without direct influence indicates a significantly increased flexibility. The molecule seems to be somewhat mobile on the surface at RT, as indicated by the jumping lines in the bottom part of the image. The profile corresponding to the orange marked line is shown in Fig. 2c. It shows a maximum height of about 300 pm and a quite uniform profile with a core

width of about 2 nm.

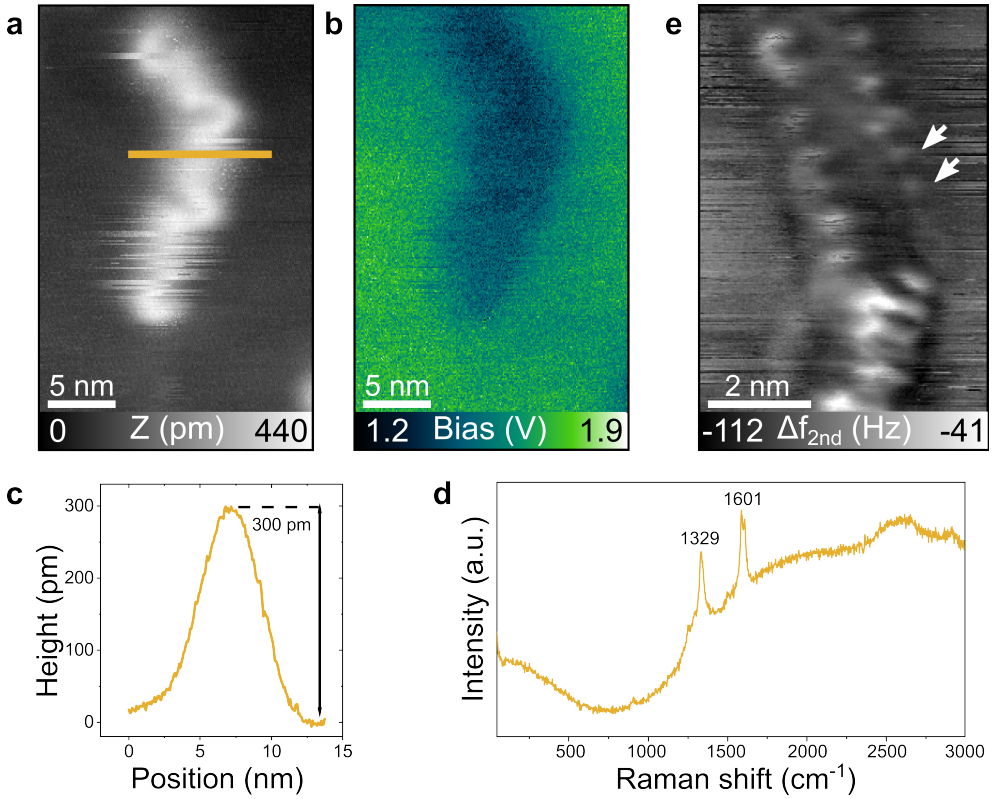

Figure 2: **Zoomed image of fjord-GNR. a,** AFM topographic image of a single FGNR. ($f_1 = 174.59$ kHz, $A_1 = 3$ nm, $\Delta f_1 = -20$ Hz), **b** Corresponding CPD image. **c,** Profile along marked line of **a**. **d,** Raman spectrum of FGNR on Au measured with laser power below 0.1 and excitation wavelength 532 nm. **e,** Second pass frequency shift image of a single FGNR ($f_1 = 163.03$ kHz, $A_1 = 5$ nm, $\Delta f_1 = -45$ Hz $z_{offset} = -300$ pm).

The contact potential difference (CPD) between the Au(111) surface and the FGNR is measured to be 500 mV as visible in the simultaneously acquired Kelvin probe force microscopy (KPFM) image of Fig. 2b. As a result we can estimate the local work function of the FGNR on Au(111) to be close to 4.8 eV. Such value is consistent with expected values of GNR on metal surfaces.[55] This higher work function value compared to a graphene monolayers measured in similar condition confirm the more p-doped state of FGNR compared to clean graphene.[56,57]

Raman spectroscopy in Fig. 2d performed after deposition on Au reveals two main peaks at 1601 and 1329 cm^{-1}, which corresponds well to spectra obtained after synthesis,[29] con-

firming the successful deposition of the ribbons.

The internal structure of the FGNR showing the repeating motive of the *tert*-butyl groups is revealed by multipass nc-AFM imaging as displayed in the second-pass frequency shift image in Fig. 2e. There, protrusions are visible on both sides of the FGNR and spaced by 850 pm, see arrows in Fig. 2e. This fits well with the distance between fjord groups of FGNR and therefore is attributed to the *tert*-butyls, attached to the side of each fjord edge.

Each protrusion likely corresponds to either two *tert*-butyls pointing upwards at the sides of the fjords or only one for each fjord, since due to steric hindrance one is most likely pointing towards the surface and can not be resolved there. A turn in the structure is also visible, in the lower part of the GNR. At the turn the *tert*-butyl protrusions are elongated and their separation distance is increased. In addition, an increase in height along with a rising slope appears, confirmed by the topography image shown in the SI Fig. S4. We attribute this to a twist of FGNR. The core is turned upwards on one side leading to the *tert*-butyl no longer being presented towards the tip and the internal structure no longer being visible. This confirms the flexible and three-dimensional nature of FGNR, allowing non-planar GNR to be obtained.

OMeCGNR adsorbs in a more flat configuration, as revealed by the topographic image of the single OMeCGNR visible in Fig. 3a. The OMeCGNR structure appears fully straight, aligned along the HB reconstruction bridges, and also more rigid as indicated by the less visible jumping lines compared to the FGNR of Fig. 2a. Notably, there are two bright elongated lobes surrounding a central darker area. The presence of the alkyl chains together with the methoxy group on the side surrounding the central flat core of the GNR is reflected in such shape. The cross section profile of the OMeCGNR is visible on Fig. 3b. There, a maximum height of 120 pm is observed. OMeCGNR is lower than the FGNR in Fig. 2c and shows uniform height along the molecule confirming a more flat structure than FGNR. The width of the OMeCGNR, with a value of 6.2 nm, is constant along the molecule, indicating a good uniformity of their structure, as indicated in the profile of Fig. 3b.

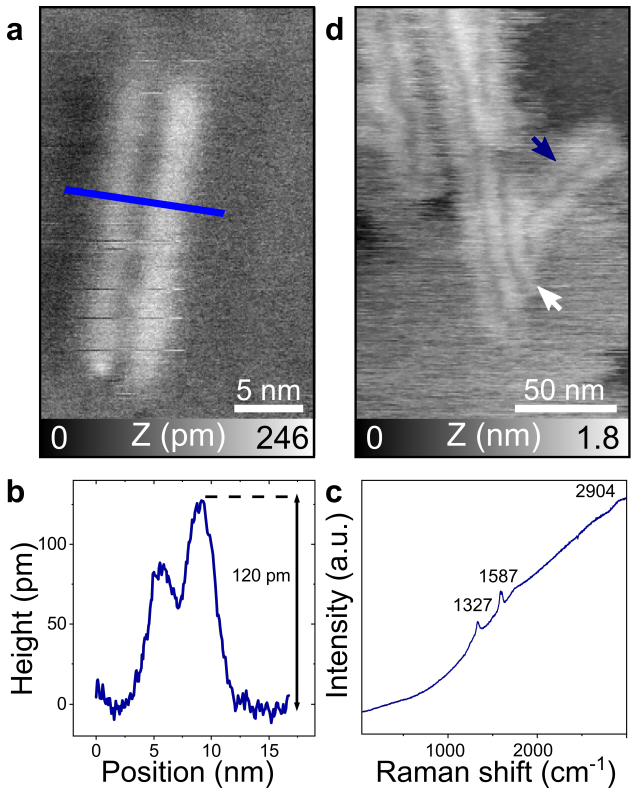

Figure 3: **Zoomed images of OMeCGNR and CGNRs. a,** nc–AFM topographic image of a single OMeCGNR. ($f_2 = 1.043$ MHz, $A_2 = 0.4$ nm, $\Delta f_2 = -30$ Hz) **b,** Profile along marked line of **a**. **c,** Raman spectrum of OMeCGNR on Au measured with laser power below 0.1 mW and excitation wavelength 532 nm. **d,** AFM topography image of CGNRs. ($f_1 = 160.0$ kHz, $A_1 = 2$ nm, $\Delta f_1 = -25$ Hz).

Raman spectrum obtained on Au is presented in Fig.3c with main peaks at 1587 and 1327 cm^{-1} in reasonable agreement with spectra after synthesis.[58]

A similar lobed structure can be observed in Fig. 3d, where five CGNRs are visible, as identified and confirmed by the excitation and torsional frequency shift images in SI Fig. S5. The core of the nanoribbon, thereby, again visible as a lower strip is surrounded by two bright lobes formed by the alkyl chains. In the center of the image only three lobes are visible for two CGNRs, indicating interdigitation of the alkyl chains. This is further reinforced by the CGNR marked with the arrows. At the white arrow it exhibits one lobe on the right and one lobe on the left, which also surrounds the GNR to its left. After a turn, at the blue arrow, it shows lobes on both sides with no more interdigitation present. The rigidity of the CGNR structure is difficult to determine. Firstly, their extended length renders a fully

straight alignment difficult, as visible in the kinks of Fig. 3d. Secondly, the interdigitation of the alkyl chains and the presence of the solvent can also influence the alignment.

Thus, our findings reveal the large influence of edge structure and functionalization to the adsorption properties of GNRs. The FGNR, due to its fjord-edge and steric hindrance of the *tert*-butyl shows a non-planar structure, as expected from its design, and also a high flexibility along with a wiggly structure on the surface. While of similar length, the OMeCGNR presents a much more rigid structure, straight and aligned with the HB reconstruction of Au(111). Their three lobed structure is uniform over their length, showing a planar structure. Similarly, the CGNRs reveal low flexibility, showing well elongated almost quite straight structures on the surface with the same two lobed structure visible from their alkyl chains and core.

GNRs on non-metallic surfaces

Obtaining GNRs on any desired surfaces in clean environment, especially when on-surface synthesis is not accessible would expand their potential applications. Aided by their more favorable solubility, the shorter deposition time of FGNR and OMeCGNR allowed us to work with non-metallic surfaces while preserving high cleanliness. FGNRs are observed on a bulk insulator crystal surface of KBr(001) after HVESD without post annealing (Fig. 4a). There, a large scale topography image of FGNR on a KBr(001) surface is shown where dispersed FGNRs are obtained on the terraces and without any preferential alignment. Surrounding them, solvent molecules and possibly KBr material are found. The HVESD is known to create defects on such surfaces that can influence the trapping of molecules.[34,47] Combined with ex-situ cleavage of the KBr before the deposition in UHV, this can explain the presence of the irregular monoatomic step edge as well as some defects influencing the FGNR stabilization. This is well visible on the 3 FGNRs adsorbed on an irregularly shaped KBr island, with a height of about 700 pm corresponding well to diatomic KBr (660 pm), visible in the top right corner of the Fig. 4a.

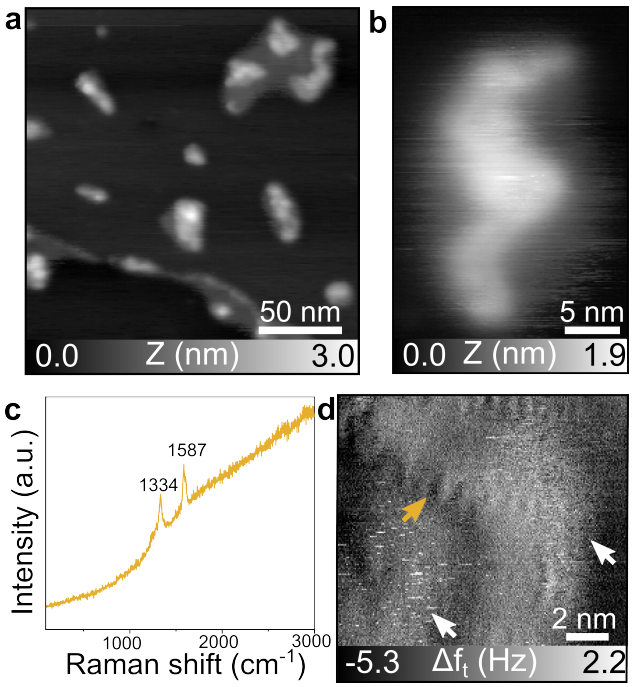

Figure 4: **FGNRs on KBr(001). a,** Large scale nc–AFM topography of FGNRs on KBr(001). (f_1 = 163.48 MHz, A_1 = 5 nm, Δf_1 = −8 Hz). **b,** nc–AFM topography image of a single FGNR on KBr(001). (f_1 = 174.59 kHz, A_1 = 3 nm, Δf_1 = −20 Hz). Corresponding torsional frequency shift image. (A_{tr} = 40 pm). **c,** Raman spectrum of FGNR on KBr(001) measured with laser power below 0.1 mW and excitation wavelength 532 nm. **d,** Zoomed torsional frequency shift image of a cluster of FGNRs (f_1 = 162.96 kHz, A_1 = 3 nm, Δf_1 = −26 Hz, A_t = 80 pm).

The wiggly structure of FGNR is also observed on KBr(001), as visible in the close-up topography image of a single continuous ribbon in Fig. 4b, confirming the flexible structure and wiggly configuration, together with the presence of slightly mobile species around the GNR. Annealing the sample did not remove the surrounding layer indicating it to be due to KBr and not solvent. Raman spectroscopy was performed to confirm the structures, as shown in Fig.4c. The expected main peaks at 1587 and 1334 cm^{-1} evidence the presence of the ribbons.[29] The internal structure of the FGNR is observed, after an annealing at 550 K. The zoomed torsional frequency shift image in Fig. 4d reveals the presence of at least two ribbons close packed together, as indicated by white arrows. Of note, are the slightly elongated regularly spaced patterns visible at the top of the image after the bend, marked by the yellow arrow. These, might again be related to the *tert*-butyls at the fjord-edges,

which in combination with the Raman spectrum gives further indication that the ribbons are intact upon deposition.

On the semi-metal HOPG, FGNRs are found to form small clusters as visible in Figs. 5a and b. In the topography image, Fig. 5a, some of the GNRs are observed to be flat lying on the surface, and some are overlapping, forming 3D cluster. Solvent is also visible around GNRs. Interestingly, even with the alignment the flexibility of the nanoribbon is still nicely present. The simultaneously acquired torsional-frequency-shift image in Fig. 5b, indicates a slight height difference after the turn (white arrow) at the bottom, the nanoribbons appear better resolved. Importantly, it can also reveal some possible indication of internal structure (blue arrow), where protrusions with a distance of about 850 pm are observed. Since the torsional mode is quite sensitive to lateral forces on flat areas, this most likely corresponds to the fjord edge and its *tert*-butyl side groups, giving indications that the GNRs were not damaged during the deposition on the non-metallic surface. This is confirmed by the Raman spectrum in Fig.5c obtained after additional depositions, which reveals the characteristic main peaks, as observed on Au and after synthesis.[29] In addition also OMeCGNR could be observed intact after deposition on HOPG in Raman spectroscopy, as shown in Fig.5d. To further confirm the versatility of the HVESD approach for accessing GNRs on further surfaces, depositions were also performed for both FGNR and OMeCGNR on SiO_2 crystals and their presence confirmed by Raman spectra presented in SI Fig. S6 and 7, respectively.

Conclusion

We showed the possibility of using HVESD to deposit different solution synthesized GNRs on various surfaces maintained in UHV conditions, with sufficient solubility limiting solvent pollution compared to other solvent-based methods. With nc-AFM we compared the structural and adsorption properties at room temperature of the GNRs on Au(111). This allows us to show a twisted, non-planar fjord-edged GNR equipped with *tert*-butyl groups with

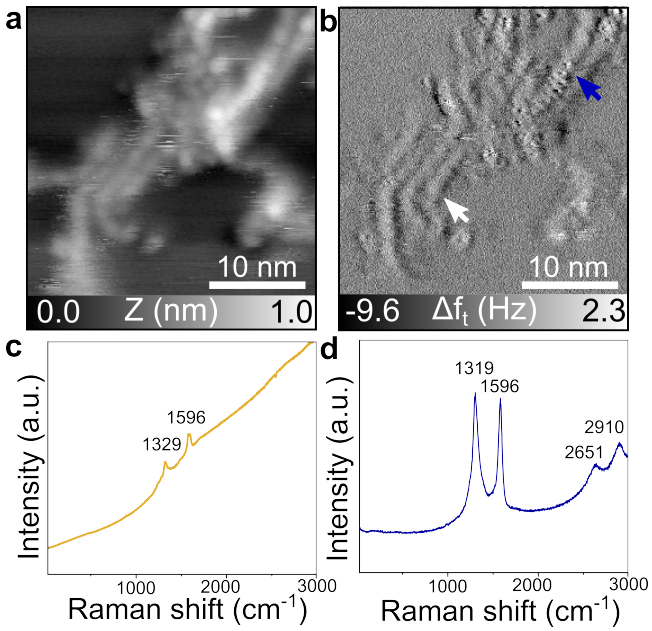

Figure 5: **GNRs on HOPG. a,** nc–AFM topography image of FGNRs on HOPG. ($f_1 = 166.3$ kHz, $A_1 = 5$ nm, $\Delta f_1 = -10$ Hz). **b,** Corresponding torsional frequency shift image. ($A_t = 40$ pm). **c,** Raman spectrum of FGNR on HOPG measured with laser power below 0.1 mW and excitation wavelength 532 nm. **d,** Raman spectrum of OMeCGNR on HOPG measured with laser power below 0.1 mW and excitation wavelength 532 nm.

a flexible and slightly wiggly structure on the surface. In contrast, we find that the two alkyl chain functionalized CGNRs, OMeCGNR additionally equipped with methoxy groups, adsorb in flat configurations agreeing well with their more rigid planar structure. Combining Raman spectroscopy and nc-AFM imaging we confirmed the presence and length distributions observed after the solution synthesis process, making HVESD a powerful method to deposit such GNRs.

The non-planar FGNR (and OMeCGNR) were also deposited on three and (two) surfaces where on-surface reaction from precursor molecules is not yet possible. Nc-AFM studies of FGNR on such surfaces confirmed the 3D shape and flexible structure. Raman spectra of FGNR and OMeCGNR confirmed their presence on further surfaces. This shows the possibility to obtain and characterize with scanning probe microscopy and Raman spectroscopy, solution synthesized GNRs on many kinds of surfaces otherwise not accessible.

Methods

Sample preparation Au(111) single crystals (Mateck GmbH) were prepared in UHV conditions by cycles of Ar^+ sputtering and annealing around 750 K. This results in atomically flat surfaces with large terraces separated by mono- to triatomic steps. KBr(111) bulk crystals were cleaved ex-situ, inserted in the system within minute and annealed to remove remaining pollutants and reduce charging effects. HOPG crystals were exfoliated ex-situ and annealed in UHV.

Molecule synthesis FGNRs were synthesized according to the procedure described in.[29] OMeCGNR synthesis is described in,[58] and CGNRs were prepared according to.[22]

Electrospray deposition The electrospray depositions were performed on samples kept at room temperature using a commercial system from MolecularSpray equipped with additional pumping stage as described in.[34] The setup was connected to the UHV preparation chamber of the room temperature nc-AFM system. The FGNRs were dissolved in toluene and methanol was added to obtain a mixture (ratio 5 to 1 in volume), while OMeCGNR and CGNR were dissolved in chlorobenzene and methanol added to form a mixture (ratio 10 to 1 in volume) due to their low solubility. During the spray deposition the pressure rose up to 1×10^{-7} mbar. Typical applied voltage were 1.8-2.3 kV adjustments being necessary to maintain spray stability. Depositions were performed for 30 min for FGNR, and 60 min for OMeCGNR and CGNR accounting for their different solubility and resulting deposition rates.

Room temperature AFM nc-AFM measurements were performed with a home-built non-contact atomic force microscope with a Nanonis RC4.5 electronics operated at room temperature. PPP-NCL cantilevers (Nanosensors) were used as sensors (typical resonance frequencies of $f_{1st} = 160$ kHz and $f_{2nd} = 1$ MHz, oscillation amplitude 2 to 5 nm and 200 to 800 pm, respectively). Their preparation consisted of an annealing for 1 h at 400 K followed

by a tip Ar^+ sputtering for 2 min at 1 keV at an Ar^+ pressure of $p = 1 \times 10^{-5}$ bar. The UHV system was maintained at a base pressure of 5×10^{-11} mbar during the measurements. The calibration of the XY-AFM scanner was checked by imaging the atomic surface lattice of a KBr(001) crystal. Multipass imaging is applied to improve the resolution by applying an offset to a recorded topography line in a second pass along each line and measuring the resulting frequency shift.[59]

Raman spectroscopy Raman spectroscopies were performed using WITec alpha300 equipped with 532 nm laser. After electrospray deposition the samples where transferred via ambient conditions to the Raman experiment. For Au(111) we used Au/Mica samples instead of Au bulk crystal.

Data availability The data that support the findings of this study are available from the corresponding authors upon reasonable request.

References

(1) Chen, Z.; Lin, Y.-M.; Rooks, M. J.; Avouris, P. Graphene Nano-Ribbon Electronics. *Phys. E* **2007**, *40*, 228–232.

(2) Ruffieux, P.; Cai, J.; Plumb, N. C.; Patthey, L.; Prezzi, D.; Ferretti, A.; Molinari, E.; Feng, X.; Müllen, K.; Pignedoli, C. A.; Fasel, R. Electronic Structure of Atomically Precise Graphene Nanoribbons. *ACS Nano* **2012**, *6*, 6930–6935.

(3) Magda, G. Z.; Jin, X.; Hagymási, I.; Vancsó, P.; Osváth, Z.; Nemes-Incze, P.; Hwang, C.; Biró, L. P.; Tapasztó, L. Room-Temperature Magnetic Order on Zigzag Edges of Narrow Graphene Nanoribbons. *Nature* **2014**, *514*, 608–611.

(4) El Abbassi, M.; Perrin, M. L.; Barin, G. B.; Sangtarash, S.; Overbeck, J.; Braun, O.; Lambert, C. J.; Sun, Q.; Prechtl, T.; Narita, A.; Müllen, K.; Ruffieux, P.; Sadeghi, H.;

Fasel, R.; Calame, M. Controlled Quantum Dot Formation in Atomically Engineered Graphene Nanoribbon Field-Effect Transistors. *ACS Nano* **2020**, *14*, 5754–5762.

(5) Liu, J.; Li, B.-W.; Tan, Y.-Z.; Giannakopoulos, A.; Sanchez-Sanchez, C.; Beljonne, D.; Ruffieux, P.; Fasel, R.; Feng, X.; Müllen, K. Toward Cove-Edged Low Band Gap Graphene Nanoribbons. *J. Am. Chem. Soc.* **2015**, *137*, 6097–6103.

(6) Fu, Y.; Yang, H.; Gao, Y.; Huang, L.; Berger, R.; Liu, J.; Lu, H.; Cheng, Z.; Du, S.; Gao, H.-J.; Feng, X. On-Surface Synthesis of NBN-Doped Zigzag-Edged Graphene Nanoribbons. *Angew. Chem., Int. Ed.* **2020**, *59*, 8873–8879.

(7) Zhou, X.; Yu, G. Modified Engineering of Graphene Nanoribbons Prepared via On-Surface Synthesis. *Adv. Mater.* **2020**, *32*, 1905957.

(8) Koen Houtsma, R. S.; de la Rie, J.; Stöhr, M. Atomically Precise Graphene Nanoribbons: Interplay of Structural and Electronic Properties. *Chem. Soc. Rev.* **2021**, *50*, 6541–6568.

(9) Cai, J.; Ruffieux, P.; Jaafar, R.; Bieri, M.; Braun, T.; Blankenburg, S.; Muoth, M.; Seitsonen, A. P.; Saleh, M.; Feng, X.; Müllen, K.; Fasel, R. Atomically Precise Bottom-up Fabrication of Graphene Nanoribbons. *Nature* **2010**, *466*, 470–473.

(10) Son, Y.-W.; Cohen, M. L.; Louie, S. G. Half-Metallic Graphene Nanoribbons. *Nature* **2006**, *444*, 347–349.

(11) Chen, Y.-C.; de Oteyza, D. G.; Pedramrazi, Z.; Chen, C.; Fischer, F. R.; Crommie, M. F. Tuning the Band Gap of Graphene Nanoribbons Synthesized from Molecular Precursors. *ACS Nano* **2013**, *7*, 6123–6128.

(12) Kawai, S.; Saito, S.; Osumi, S.; Yamaguchi, S.; Foster, A. S.; Spijker, P.; Meyer, E. Atomically Controlled Substitutional Boron-Doping of Graphene Nanoribbons. *Nat. Commun.* **2015**, *6*, 8098.

(13) Ruffieux, P.; Wang, S.; Yang, B.; Sánchez-Sánchez, C.; Liu, J.; Dienel, T.; Talirz, L.; Shinde, P.; Pignedoli, C. A.; Passerone, D.; Dumslaff, T.; Feng, X.; Müllen, K.; Fasel, R. On-Surface Synthesis of Graphene Nanoribbons with Zigzag Edge Topology. *Nature* **2016**, *531*, 489–492.

(14) Yang, H.; Gao, Y.; Niu, W.; Chang, X.; Huang, L.; Liu, J.; Mai, Y.; Feng, X.; Du, S.; Gao, H.-J. Fabrication of Sulfur-Doped Cove-Edged Graphene Nanoribbons on Au(111). *Chinese Phys. B* **2021**, *30*, 077306.

(15) Kittelmann, M.; Nimmrich, M.; Lindner, R.; Gourdon, A.; Kühnle, A. Sequential and Site-Specific On-Surface Synthesis on a Bulk Insulator. *ACS Nano* **2013**, *7*, 5614–5620.

(16) Ma, C.; Xiao, Z.; Zhang, H.; Liang, L.; Huang, J.; Lu, W.; Sumpter, B. G.; Hong, K.; Bernholc, J.; Li, A.-P. Controllable Conversion of Quasi-Freestanding Polymer Chains to Graphene Nanoribbons. *Nat. Commun.* **2017**, *8*, 14815.

(17) Kolmer, M.; Steiner, A.-K.; Izydorczyk, I.; Ko, W.; Engelund, M.; Szymonski, M.; Li, A.-P.; Amsharov, K. Rational Synthesis of Atomically Precise Graphene Nanoribbons Directly on Metal Oxide Surfaces. *Science* **2020**, *369*, 571–575.

(18) Wang, S.; Talirz, L.; Pignedoli, C. A.; Feng, X.; Müllen, K.; Fasel, R.; Ruffieux, P. Giant Edge State Splitting at Atomically Precise Graphene Zigzag Edges. *Nat. Commun.* **2016**, *7*, 11507.

(19) Deniz, O.; Sánchez-Sánchez, C.; Dumslaff, T.; Feng, X.; Narita, A.; Müllen, K.; Kharche, N.; Meunier, V.; Fasel, R.; Ruffieux, P. Revealing the Electronic Structure of Silicon Intercalated Armchair Graphene Nanoribbons by Scanning Tunneling Spectroscopy. *Nano Lett.* **2017**, *17*, 2197–2203.

(20) Jacobse, P. H.; Mangnus, M. J. J.; Zevenhuizen, S. J. M.; Swart, I. Mapping the Conductance of Electronically Decoupled Graphene Nanoribbons. *ACS Nano* **2018**, *12*, 7048–7056.

(21) Yang, X.; Dou, X.; Rouhanipour, A.; Zhi, L.; Räder, H. J.; Müllen, K. Two-Dimensional Graphene Nanoribbons. *J. Am. Chem. Soc.* **2008**, *130*, 4216–4217.

(22) Narita, A.; Feng, X.; Hernandez, Y.; Jensen, S. A.; Bonn, M.; Yang, H.; Verzhbitskiy, I. A.; Casiraghi, C.; Hansen, M. R.; Koch, A. H., et al. Synthesis of Structurally Well-Defined and Liquid-Phase-Processable Graphene Nanoribbons. *Nat. Chem.* **2014**, *6*, 126–132.

(23) Narita, A.; Wang, X.-Y.; Feng, X.; Müllen, K. New Advances in Nanographene Chemistry. *Chem. Soc. Rev.* **2015**, *44*, 6616–6643.

(24) Narita, A.; Chen, Z.; Chen, Q.; Müllen, K. Solution and On-Surface Synthesis of Structurally Defined Graphene Nanoribbons as a New Family of Semiconductors. *Chem. Sci.* **2019**, *10*, 964–975.

(25) Daigle, M.; Miao, D.; Lucotti, A.; Tommasini, M.; Morin, J.-F. Helically Coiled Graphene Nanoribbons. *Angew. Chem., Int. Ed.* **2017**, *56*, 6213–6217.

(26) Castro-Fernández, S.; Cruz, C. M.; Mariz, I. F. A.; Márquez, I. R.; Jiménez, V. G.; Palomino-Ruiz, L.; Cuerva, J. M.; Maçôas, E.; Campaña, A. G. Two-Photon Absorption Enhancement by the Inclusion of a Tropone Ring in Distorted Nanographene Ribbons. *Angew. Chem., Int. Ed.* **2020**, *59*, 7139–7145.

(27) Niu, W.; Ma, J.; Soltani, P.; Zheng, W.; Liu, F.; Popov, A. A.; Weigand, J. J.; Komber, H.; Poliani, E.; Casiraghi, C.; Droste, J.; Hansen, M. R.; Osella, S.; Beljonne, D.; Bonn, M.; Wang, H. I.; Feng, X.; Liu, J.; Mai, Y. A Curved Graphene Nanoribbon with Multi-Edge Structure and High Intrinsic Charge Carrier Mobility. *J. Am. Chem. Soc.* **2020**, *142*, 18293–18298.

(28) Ma, S.; Gu, J.; Lin, C.; Luo, Z.; Zhu, Y.; Wang, J. Supertwistacene: A Helical Graphene Nanoribbon. *J. Am. Chem. Soc.* **2020**, *142*, 16887–16893.

(29) Yao, X.; Zheng, W.; Osella, S.; Qiu, Z.; Fu, S.; Schollmeyer, D.; Müller, B.; Beljonne, D.; Bonn, M.; Wang, H. I.; Müllen, K.; Narita, A. Synthesis of Nonplanar Graphene Nanoribbon with Fjord Edges. *J. Am. Chem. Soc.* **2021**, *143*, 5654–5658.

(30) Kawai, S.; Krejčí, O.; Nishiuchi, T.; Sahara, K.; Kodama, T.; Pawlak, R.; Meyer, E.; Kubo, T.; Foster, A. S. Three-Dimensional Graphene Nanoribbons as a Framework for Molecular Assembly and Local Probe Chemistry. *Sci. Adv.* **2020**,

(31) Vo, T. H.; Shekhirev, M.; Kunkel, D. A.; Morton, M. D.; Berglund, E.; Kong, L.; Wilson, P. M.; Dowben, P. A.; Enders, A.; Sinitskii, A. Large-Scale Solution Synthesis of Narrow Graphene Nanoribbons. *Nat. Commun.* **2014**, *5*, 3189.

(32) Radocea, A.; Sun, T.; Vo, T. H.; Sinitskii, A.; Aluru, N. R.; Lyding, J. W. Solution-Synthesized Chevron Graphene Nanoribbons Exfoliated onto H:Si(100). *Nano Lett.* **2017**, *17*, 170–178.

(33) McCurdy, R. D.; Jacobse, P. H.; Piskun, I.; Veber, G. C.; Rizzo, D. J.; Zuzak, R.; Mutlu, Z.; Bokor, J.; Crommie, M. F.; Fischer, F. R. Synergetic Bottom-Up Synthesis of Graphene Nanoribbons by Matrix-Assisted Direct Transfer. *J. Am. Chem. Soc.* **2021**, *143*, 4174–4178.

(34) Hinaut, A.; Pawlak, R.; Meyer, E.; Glatzel, T. Electrospray Deposition of Organic Molecules on Bulk Insulator Surfaces. *Beilstein J. Nanotechnol.* **2015**, *6*, 1927–1934.

(35) Erler, P.; Schmitt, P.; Barth, N.; Irmler, A.; Bouvron, S.; Huhn, T.; Groth, U.; Pauly, F.; Gragnaniello, L.; Fonin, M. Highly Ordered Surface Self-Assembly of Fe4 Single Molecule Magnets. *Nano Lett.* **2015**, *15*, 4546–4552.

(36) Hinaut, A.; Meier, T.; Pawlak, R.; Feund, S.; Jöhr, R.; Kawai, S.; Glatzel, T.; Decurtins, S.; Müllen, K.; Narita, A.; Liu, S.-X.; Meyer, E. Electrospray Deposition of Structurally Complex Molecules Revealed by Atomic Force Microscopy. *Nanoscale* **2018**, *10*, 1337–1344.

(37) Scherb, S.; Hinaut, A.; Pawlak, R.; Vilhena, J. G.; Liu, Y.; Freund, S.; Liu, Z.; Feng, X.; Müllen, K.; Glatzel, T.; Narita, A.; Meyer, E. Giant Thermal Expansion of a Two-Dimensional Supramolecular Network Triggered by Alkyl Chain Motion. *Commun. Mater.* **2020**, *1*, 1–7.

(38) Rauschenbach, S.; Stadler, F. L.; Lunedei, E.; Malinowski, N.; Koltsov, S.; Costantini, G.; Kern, K. Electrospray Ion Beam Deposition of Clusters and Biomolecules. *Small* **2006**, *2*, 540–547.

(39) Satterley, C. J.; Perdigão, L. M. A.; Saywell, A.; Magnano, G.; Rienzo, A.; Mayor, L. C.; Dhanak, V. R.; Beton, P. H.; O'Shea, J. N. Electrospray Deposition of Fullerenes in Ultra-High Vacuum:In Situ Scanning Tunneling Microscopy and Photoemission Spectroscopy. *Nanotechnology* **2007**, *18*, 455304.

(40) Hauptmann, N.; Hamann, C.; Tang, H.; Berndt, R. Switching and Charging of a Ruthenium Dye on Ag(111). *Phys. Chem. Chem. Phys.* **2013**, *15*, 10326–10330.

(41) Rinke, G.; Rauschenbach, S.; Schrettl, S.; Hoheisel, T. N.; Blohm, J.; Gutzler, R.; Rosei, F.; Frauenrath, H.; Kern, K. Soft-Landing Electrospray Ion Beam Deposition of Sensitive Oligoynes on Surfaces in Vacuum. *Int. J. Mass Spectrom.* **2015**, *377*, 228–234.

(42) Kondratuk, D. V.; Perdigão, L. M.; Esmail, A. M.; O'Shea, J. N.; Beton, P. H.; Anderson, H. L. Supramolecular Nesting of Cyclic Polymers. *Nat. Chem.* **2015**, *7*, 317.

(43) Gragnaniello, L.; Paschke, F.; Erler, P.; Schmitt, P.; Barth, N.; Simon, S.; Brune, H.; Rusponi, S.; Fonin, M. Uniaxial 2D Superlattice of Fe4 Molecular Magnets on Graphene. *Nano Lett.* **2017**, *17*, 7177–7182.

(44) Jasper-Tönnies, T.; Gruber, M.; Karan, S.; Jacob, H.; Tuczek, F.; Berndt, R. Deposition of a Cationic Fe III Spin-Crossover Complex on Au(111): Impact of the Counter Ion. *J. Phys. Chem. Lett.* **2017**, *8*, 1569–1573.

(45) Krumbein, L.; Anggara, K.; Stella, M.; Michnowicz, T.; Ochner, H.; Abb, S.; Rinke, G.; Portz, A.; Dürr, M.; Schlickum, U.; Baldwin, A.; Floris, A.; Kern, K.; Rauschenbach, S. Fast Molecular Compression by a Hyperthermal Collision Gives Bond-Selective Mechanochemistry. *Phys. Rev. Lett.* **2021**, *126*, 056001.

(46) Ran, W.; Walz, A.; Stoiber, K.; Knecht, P.; Xu, H.; Papageorgiou, A. C.; Huettig, A.; Cortizo-Lacalle, D.; Mora-Fuentes, J. P.; Mateo-Alonso, A.; Schlichting, H.; Reichert, J.; Barth, J. V. Depositing Molecular Graphene Nanoribbons on Ag(111) by Electrospray Controlled Ion Beam Deposition: Self-Assembly and On-Surface Transformations. *Angew. Chem. Int. Ed.* **2022**, *61*, e202111816.

(47) Hinaut, A.; Scherb, S.; Freund, S.; Liu, Z.; Glatzel, T.; Meyer, E. Influence of Electrospray Deposition on C60 Molecular Assemblies. *Beilstein J. Nanotechnol.* **2021**, *12*, 552–558.

(48) Gillen, R.; Mohr, M.; Maultzsch, J. Raman-Active Modes in Graphene Nanoribbons. *physica status solidi (b)* **2010**, *247*, 2941–2944.

(49) Han, P.; Akagi, K.; Federici Canova, F.; Shimizu, R.; Oguchi, H.; Shiraki, S.; Weiss, P. S.; Asao, N.; Hitosugi, T. Self-Assembly Strategy for Fabricating Connected Graphene Nanoribbons. *ACS Nano* **2015**, *9*, 12035–12044.

(50) Senkovskiy, B. V.; Usachov, D. Y.; Fedorov, A. V.; Marangoni, T.; Haberer, D.; Tresca, C.; Profeta, G.; Caciuc, V.; Tsukamoto, S.; Atodiresei, N.; Ehlen, N.; Chen, C.; Avila, J.; Asensio, M. C.; Varykhalov, A. Y.; Nefedov, A.; Wöll, C.; Kim, T. K.; Hoesch, M.; Fischer, F. R. et al. Boron-Doped Graphene Nanoribbons: Electronic Structure and Raman Fingerprint. *ACS Nano* **2018**, *12*, 7571–7582.

(51) Kim, J.; Lee, N.; Min, Y. H.; Noh, S.; Kim, N.-K.; Jung, S.; Joo, M.; Yamada, Y. Distinguishing Zigzag and Armchair Edges on Graphene Nanoribbons by X-ray Photoelectron and Raman Spectroscopies. *ACS Omega* **2018**, *3*, 17789–17796.

(52) Preis, T.; Kick, C.; Lex, A.; Weiss, D.; Eroms, J.; Narita, A.; Hu, Y.; Müllen, K.; Watanabe, K.; Taniguchi, T. Graphene Nanoribbons on Hexagonal Boron Nitride: Deposition and Transport Characterization. *Appl. Phys. Lett.* **2019**, *114*, 173101.

(53) Tahara, K.; Lei, S.; Adisoejoso, J.; De Feyter, S.; Tobe, Y. Supramolecular Surface-Confined Architectures Created by Self-Assembly of Triangular Phenylene–Ethynylene Macrocycles via van Der Waals Interaction. *Chem. Commun.* **2010**, *46*, 8507–8525.

(54) van der Lit, J.; Jacobse, P. H.; Vanmaekelbergh, D.; Swart, I. Bending and Buckling of Narrow Armchair Graphene Nanoribbons via STM Manipulation. *New J. Phys.* **2015**, *17*, 053013.

(55) Bronner, C.; Haase, A.; Tegeder, P. Image Potential States at Chevron-Shaped Graphene Nanoribbons /Au(111) Interfaces. *Phys. Rev. B* **2015**, *91*, 045428.

(56) Khomyakov, P. A.; Giovannetti, G.; Rusu, P. C.; Brocks, G.; van den Brink, J.; Kelly, P. J. First-Principles Study of the Interaction and Charge Transfer between Graphene and Metals. *Phys. Rev. B* **2009**, *79*, 195425.

(57) Schulzendorf, M.; Hinaut, A.; Kisiel, M.; Jöhr, R.; Pawlak, R.; Restuccia, P.; Meyer, E.; Righi, M. C.; Glatzel, T. Altering the Properties of Graphene on Cu(111) by Intercalation of Potassium Bromide. *ACS Nano* **2019**, *13*, 5485–5492.

(58) Götz, A.; Wang, X.-Y.; Ruini, A.; Zheng, W.; Soltani, P.; Graf, R.; Tries, A.; Li, J.; Palma, C.-A.; Molinari, E.; Hansen, M. R.; Wang, H. I.; Prezzi, D.; Müllen, K.; Narita, A. Band Structure Modulation by Methoxy-Functionalization of Graphene Nanoribbons. *J. Mater. Chem. C* **2022**, *10*, 4173–4181.

(59) Iwata, K.; Yamazaki, S.; Mutombo, P.; Hapala, P.; Ondráček, M.; Jelínek, P.; Sugimoto, Y. Chemical Structure Imaging of a Single Molecule by Atomic Force Microscopy at Room Temperature. *Nat. Commun.* **2015**, *6*, 7766.

Acknowledgement

Se.S., A.H., Th.G. and E.M. thank the Swiss National Science Foundation (SNF) and the Swiss Nanoscience Institute (SNI). E.M., Y.S. and Se.S. thank the funding from the European Research Council (ERC) under the European Union's Horizon 2020 research and innovation program (ULTRADISS grant agreement No. [834402]). K.M. acknowledges a fellowship from Gutenberg Research College, Johannes Gutenberg University Mainz. X.Y., A.G., X.W., Y.H., Z.Q., K.M. and A.N. thank the financial support by the Max Planck Society. A.N. is grateful to the funding from the FLAG-ERA Grant OPERA by DFG 437130745 and the ANR-DFG NLE Grant GRANAO by DFG 431450789.

Authors contribution

E.M. and A.H. conceived the experiments. Se.S. performed spray depositions. Se.S. and A.H. performed the AFM measurements at room temperature. A.N., X.Y., A.G., X.W., Y.H. and Z.Q. synthesized the GNRs. S.H. performed Raman spectroscopy. Se.S. and A.H. wrote the manuscript. Se.S., A.H., X.Y., A.G., S.H., X.W., Y.H., Z.Q., Y.S., K.M., Th.G., A.N. and E.M. read and discussed the manuscript.

Correspondence and requests for materials should be addressed to E.M. (email: ernst.meyer@unibas.ch)

Competing interests: The authors declare no competing interests.

Supplementary information

The following files are available online.

Supplementary Fig. 1: Contrast modified topography image of FGNR alignment on Au(111).

Supplementary Fig. 2: Contrast modified topography image of OMeCGNR alignment on Au(111).

Supplementary Fig. 3: Excitation image of Figure 1f identifying different domains on the surface.

Supplementary Fig. 4: Topography nc-AFM image of non-planarity of FGNR in the first pass of Figure 2c.

Supplementary Fig. 5: Excitation and torsional frequency shift images of Figure 3b.

Supplementary Fig. 6: Raman spectrum of FGNR on SiO_2 measured with laser power below 0.1 mW and excitation wavelength 532 nm.

Supplementary Fig. 7: Raman spectrum of OMeCGNR on SiO_2 measured with laser power below 0.1 mW and excitation wavelength 532 nm.